Overview of the Large 25 April 2015 Gorkha, Nepal, Earthquake from Accelerometric Perspectives

by M. Bhattarai, L. B. Adhikari, U. P. Gautam, A. Laurendeau, C. Labonne, R. Hoste-Colomer, O. Sèbe, and B. Hernandez

ABSTRACT

Central Nepal was struck on 25 April 2015 by the M_w 7.8 (M_L 7.6) Gorkha earthquake, which initiated about 80 km northwest of Kathmandu and ruptured toward the east along a 140-km-long west-northwest–east-southeast fault segment. Kathmandu basin, located about halfway along the ruptured segment a few kilometers from the southernmost fault tip, was strongly affected. In this article, we present a preliminary analysis of the acceleration-time histories of the 25 April 2015 M_w 7.8 mainshock and the 12 May 2015 M_w 7.3 (M_L 6.8) aftershock recorded at the Department of Mines and Geology office building in central Kathmandu valley. We analyze their frequency content using Stockwell *et al.* (1996) time–frequency decomposition and a polarization analysis (Pinnegar, 2006). We then compute their strong-motion parameters and finally compare their spectral accelerations with the Boore and Atkinson (2008) ground-motion prediction equation.

Online Material: Raw accelerometric data at station DMG for the 25 April mainshock, the 25 and 26 April aftershocks and the 12 May aftershock, and preliminary analysis of signals recorded at station_NQ.KATNP.

THE 2015 GORKHA EARTHQUAKE AND MAJOR AFTERSHOCKS

The Gorkha earthquake occurred on 25 April at 06:11 UTC (11: 56 Nepal Standard Time). It is the most devastating seismic event in Nepal since the great 1934 earthquake (M_w 8.4). It was widely felt in Nepal and neighboring countries (India, China, and Bangladesh). The intensity of the shaking in the Kathmandu valley was strong, with reported macroseismic intensities generally around VI–VII on the European Macroseismic Scale (EMS) (Martin *et al.*, 2015). As a result, the seismic event caused 8778 fatalities and 22,303 injuries, and more than 790,000 buildings were fully or partially damaged in Nepal (Government of Nepal, 2015, http://drrportal.gov.np/, last accessed June 2015). It triggered numerous landslides, avalanches, and rockslides above and near the rupture zone.

The mainshock epicenter was located near Barpak village, Gorkha district, 80 km northwest of Kathmandu. The local magnitude reported by the National Seismological Center of Nepal (NSC) was M_L 7.6, and the final moment magnitude was M_w 7.8 according to the U.S. Geological Survey (USGS). The earthquake ruptured a segment of the Main Himalayan thrust (MHT). This plate boundary megathrust accommodates about 20 mm/yr of the convergence between the Indian and Eurasian plates (~40 mm/yr; Lavé and Avouac, 2000; Jouanne *et al.*, 2004; Bettinelli *et al.*, 2006; Ader *et al.*, 2012). The focal mechanism displays a purely thrust-faulting motion consistent with reverse-fault displacement of the MHT (Commissariat à l'énergie atomique et aux énergies alternatives [CEA], 2015).

The mainshock rupture is delineated by the aftershocks, a result consistent with preliminary finite-source modeling using Interferometric Synthetic Aperture Radar, seismological data, and continuous Global Positioning System (Avouac *et al.*, 2015; Galetzka *et al.*, 2015). From 25 April to 11 May, 260 aftershocks with $M_L \geq 4.0$ were located by the NSC (Adhikari *et al.*, 2015). A second major event took place on 12 May 2015 at 07:05 UTC, with M_L of 6.8 (NSC) and M_w 7.3 (USGS). This event is located at the eastern edge of the mainshock rupture zone (Fig. 1).

THE DMG ACCELEROMETRIC STATION

One accelerometer (DMG), installed in the premises of the Department of Mines and Geology in Lainchaur, Kathmandu (85.3166° E, 27.7193° N), recorded the mainshock and aftershocks. The accelerometric station considered here was installed to complement the existing National Seismological Center Network (Fig. 1). The station is instrumented with a Geosig-AC23 sensor and a GSR24 digitizer (Bhattarai *et al.*, 2011) installed on a concrete slab in a single-story building. Complementary non-telemetered stations have been deployed in the past (Bhattarai

 doi: 10.1785/0220150140

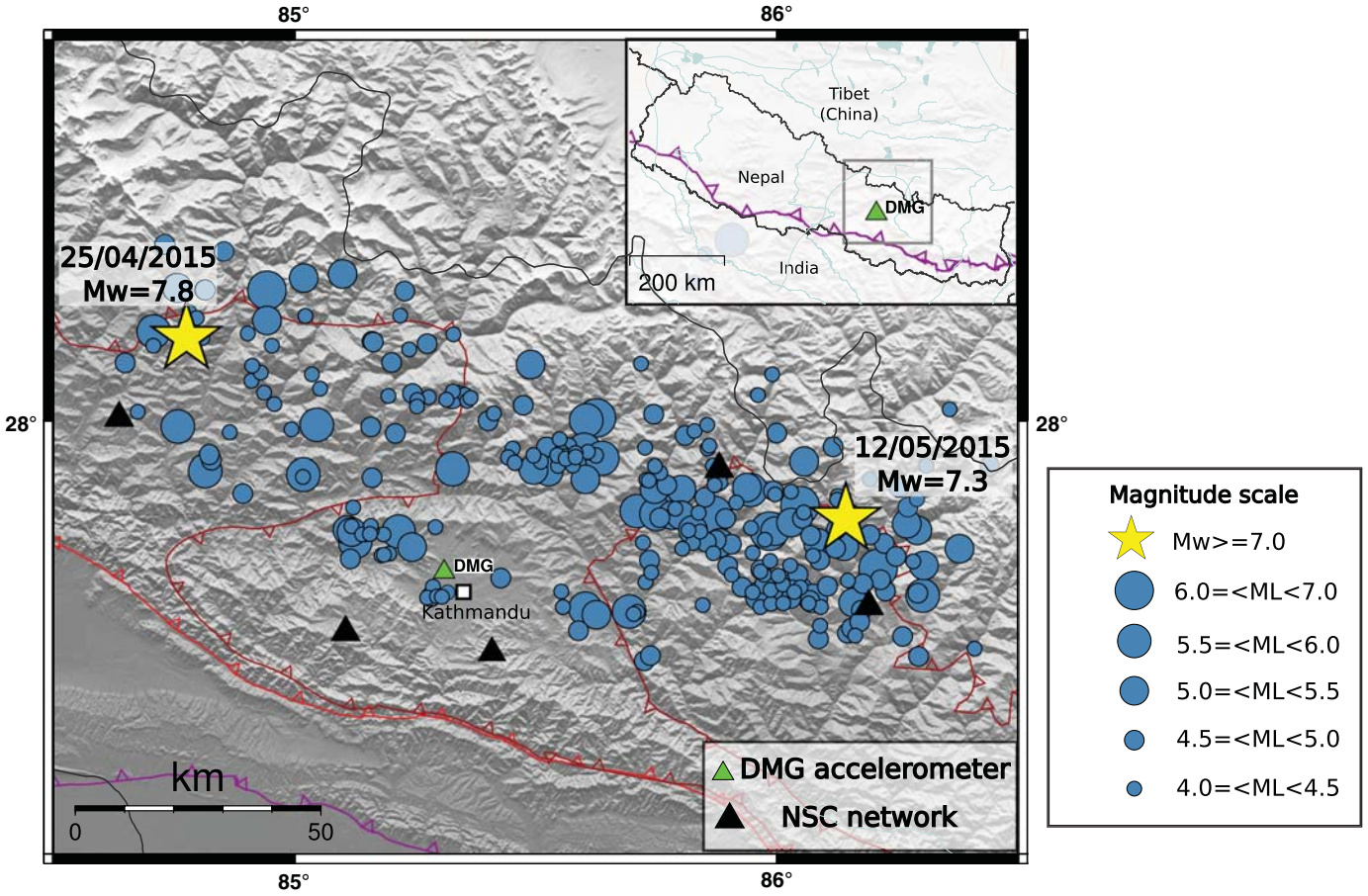

▲ **Figure 1.** The seismic stations (black triangles) and the DMG accelerometric station (green triangle). Yellow stars show the location of the mainshock and the major aftershock. The mainshock occurred on 25 April 2015; its epicenter is located at the western part of the seismic sequence. Blue circles show the location of the aftershocks with magnitude greater than 4.0 until 14 May 2015.

et al., 2011). However, some were out of service and some remain unvisited because of the mainshock, given the recent workload at the NSC. The DMG station is located at the center of the Kathmandu valley, a basin filled by Pleistocene and Quaternary lacustrine, alluvial fan, and fluvial deposits. The sediments reach a depth of 500 m at DMG and rest on a metasedimentary Pre-Cambrian to Paleozoic bedrock (Sakai, 2001). Boreholes drilled nearby corroborate this subsurface geology. However, to our knowledge, no geophysical data characterizing the local shear-wave velocity or the site response at DMG are presently available. Because of that lack, we use later estimates of the average shear-wave velocity over the upper 30 m (V_{S30}) derived from a relationship between the topographic slope and V_{S30} (Wald and Allen, 2007). The V_{S30} maps and grid are available on the USGS website (http://earthquake.usgs.gov/hazards/apps/vs30/, last accessed June 2015). At the DMG location, V_{S30} is estimated at ~250 m/s. We are aware of the limitations of this method; however, the V_{S30} value is consistent with the range of V_{S30} values estimated by Japan International Cooperation Agency (JICA, 2002) to be between 180 and 310 m/s for the Kathmandu basin. In addition, Paudyal *et al.* (2012) estimated the horizontal-to-vertical spectral ratios (HVSRs) from microtremors (method introduced by Nakamura, 1989) for a grid of 171 points around Kathmandu. These authors estimated dominant periods to be between 0.5 and 1 Hz in the vicinity of DMG. Their study is reliable only for frequencies larger than 0.5 Hz.

GROUND-MOTION OBSERVATION OF THE TWO MAIN EVENTS AT DMG STATION

In this section, we describe the strong ground motion records from DMG station for the Gorkha M_w 7.8 mainshock and the 12 May 2015 M_w 7.3 aftershock by considering the time histories, the frequency content, the time–frequency decomposition, and the polarization. For the other aftershocks with $M_L > 6.5$, the strong-motion parameters are computed following Bhattarai *et al.* (2011) and are given in Table 1 (Ⓔ the raw accelerometric records are provided in the electronic supplement to this article). NQ.KATNP, another accelerometric station located in Kathmandu, recorded the seismic sequence; the accelerograms recorded at this station are publicly available (http://www.strongmotioncenter.org, last accessed June 2015) and have been analyzed by Goda *et al.* (2015) and Dixit *et al.*

Table 1
Main Characteristics of the Events with M_L >6.5 Associated with the 25 April M_w 7.8 Gorkha Earthquake

Event ID	Station	M_L/M_w	R_{epi} (km)	Components	PGA (cm/s^2)	PGV (cm/s)	I_A (m/s)	CAV (m/s)	I_H (cm)	Dsr (5%–95%) (s)
20150425_061140	DMG	7.6/7.8	80	N	174	58.7	1.02	16.9	95.7	48
20150425_061140	DMG	7.6/7.8	80	W	124	62.7	1.12	18.2	102.0	46
20150425_061140	DMG	7.6/7.8	80	D	202	30.1	1.38	17.2	66.8	36
20150425_0645	DMG	6.6/6.6	85	N	63.7	5.56	4.98	2.96	33.2	34
20150425_0645	DMG	6.6/6.6	85	W	62.2	11.1	9.92	3.98	56.1	27
20150425_0645	DMG	6.6/6.6	85	D	32.3	3.74	2.54	2.27	22.7	35
20150426_0709	DMG	6.9/6.7	73	N	57.4	6.86	12.3	6.04	34.7	48
20150426_0709	DMG	6.9/6.7	73	W	58.4	9.42	14.8	6.70	39.8	47
20150426_0709	DMG	6.9/6.7	73	D	44.3	3.65	6.22	4.39	24.2	48
20150512_0705	DMG	6.8/7.3	80	N	82.7	10.4	23.3	8.61	50.1	45
20150512_0705	DMG	6.8/7.3	80	W	120	17.7	33.2	9.65	82.5	36
20150512_0705	DMG	6.8/7.3	80	D	54.9	8.57	10.5	5.73	36.7	41

Ⓔ These raw accelerometric data are provided in the electronic supplement.

Event ID corresponds to the event date defined as YYYYMMDD_HHMM; M_L/M_w, local/moment magnitudes; R_{epi}, epicentral distance; Components of the signal are N (north), W (west), and D (down); PGA, peak ground acceleration; PGV, peak ground velocity; I_A, Arias intensity; CAV, cumulative absolute velocity; I_H, Housner intensity; Dsr, significant relative duration.

(2015). We analyzed the NQ.KATNP data using a process similar to that used for the DMG station and present the analysis in Ⓔ Figures S1–S3.

Time History Analysis (Fig. 2)

A simple processing is applied to the raw acceleration-time histories recorded at DMG. The first 100 and 70 s of signal are extracted for the mainshock and for the aftershock, respectively. The signal is tapered with a 5% cosine taper. Then, the acceleration-time histories are analyzed and the main strong-motion parameters computed. Horizontal and vertical acceleration-time histories of these two events are shown in Figure 2.

The mainshock records have a peak ground acceleration (PGA) of 0.15g for the geometrical mean of the two horizontal components, with a larger PGA of 0.21g on the vertical component. Thus, the vertical-to-horizontal ratio is 1.4. Figure 2 presents a quantification of the strong ground motion duration using the normalized Husid diagram (Husid, 1969), which represents the cumulative Arias intensity (I_A) over time, a measure of the signal energy (Arias, 1970). A common duration parameter is the significant relative duration (noted as Dsr(5%–95%)) (e.g., Bommer *et al.*, 2009), which is the time interval between 5% and 95% of the cumulative I_A over time. Dsr(5%–95%) is around 42 s for the horizontal components and around 35 s for the vertical one. The energy is mainly accumulated between 21 and 37 s. The horizontal components are mainly characterized by a low-frequency signal from 23 s.

Time histories of the aftershock recorded at DMG show PGAs of 0.10g and 0.06g for the horizontal and the vertical components, respectively. Dsr(5%–95%) is around 28 s for the horizontal components and around 33 s for the vertical one. The energy is mainly accumulated between 13 and 26 s.

For both the mainshock and the aftershock, a second energy pulse in the *S*-wave part is observed on the north component: ~44 s for the mainshock and ~32 s for the aftershock. This is observable especially with the Husid plots, which present a rapid increase at these times. The NQ.KATNP records reveal the same arrivals (Ⓔ Fig. S1).

Spectral Content (Fig. 3)

Figure 3 shows the Fourier acceleration spectra (FAS) for each component. For the mainshock, the predominant period of the horizontal component is ~0.23 Hz. The vertical spectrum is flatter and more consistent with a Brune model spectrum (Brune, 1970, 1971) with an apparent corner frequency slightly above 0.1 Hz. The large amplitude on the horizontal component (~0.23 Hz) may be related to a Kathmandu basin site effect and/or properties of the source. A classical way to estimate site effects is to consider spectral ratios of ground-motion recordings. The HVSR potentially highlights the predominant periods of amplification resulting from strong impedance contrasts (e.g., Lermo and Chavez-Garcia, 1993). The HVSR of the mainshock exhibits a clear peak at 0.2 Hz (Fig. 3).

For the 12 May aftershock, we also observe amplification at frequencies between 0.2 and 0.3 Hz, but the peak is less sharply defined. HVSRs also reveal amplification around 2–3 Hz, which is not visible on the mainshock HVSRs. For the FAS, the maximum is reached around 1 Hz. The vertical component reveals a corner frequency of ~0.4 Hz.

The vertical-component FAS presents a larger amplitude at high frequency for both events.

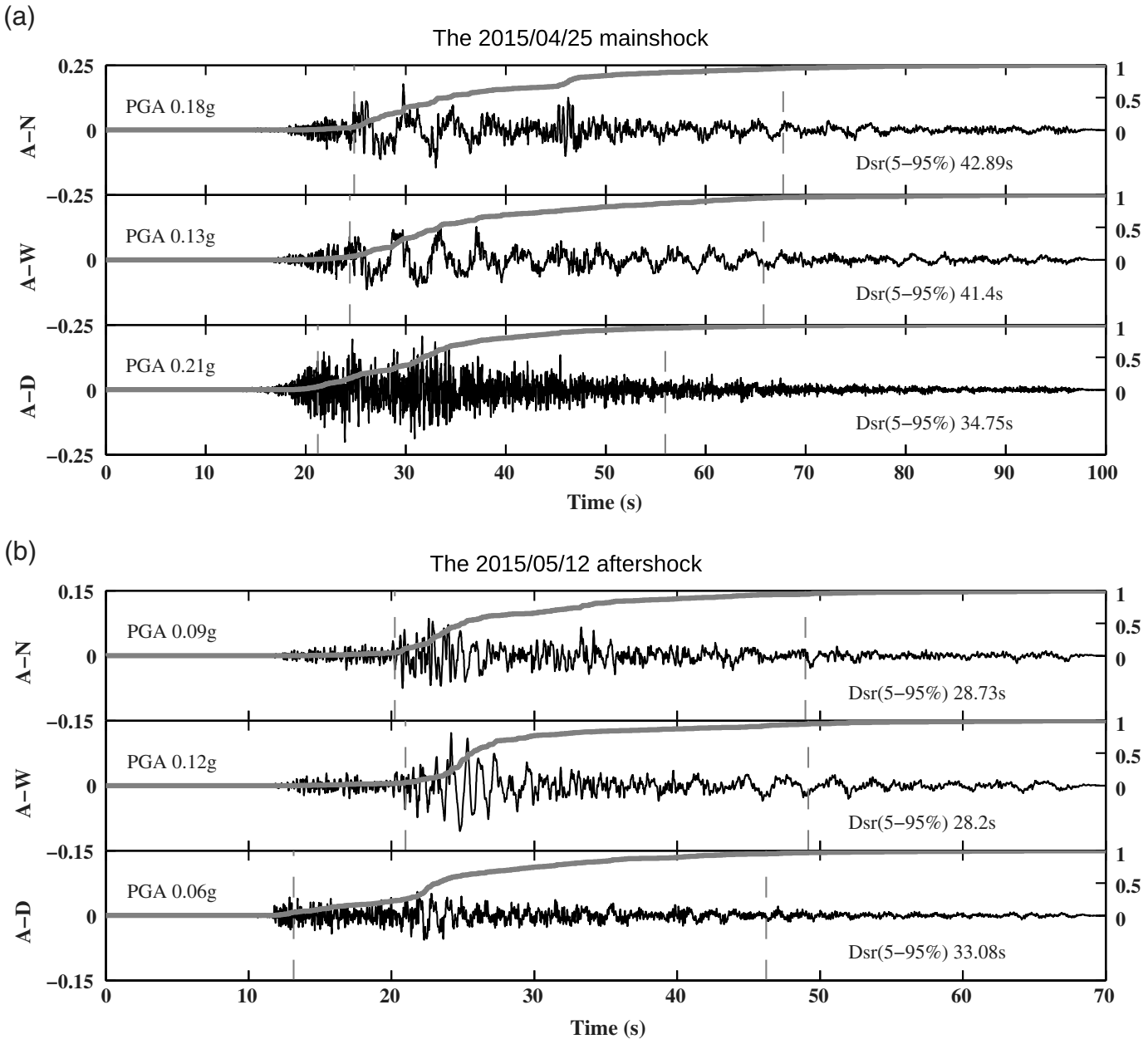

▲ **Figure 2.** Acceleration-time histories in *g* at the DMG station (a) for the 25 April M_w 7.8 mainshock and (b) for the 12 May M_w 7.3 aftershock. N, W, and D correspond, respectively, to north, west, and down components. The normalized Husid diagrams are represented on the second axis (gray solid lines). The time corresponding to 5% and 95% of the cumulative Arias intensity is also represented (dashed gray lines). The peak ground acceleration (PGA) and significant relative duration Dsr(5%–95%) are also indicated for each component.

Time–Frequency and Polarization Analysis (Fig. 4)

An analysis of three-component signals can provide an estimate of polarization characteristics of seismic wavefields. The polarization characteristics help with understanding the seismic-wavefield composition and discriminating between the different types of waves based on their degree of ellipticity or the orientation of their polarization plane. Here, the time–frequency representation is incorporated in the polarization analysis, and the polarization attributes are estimated directly from the three components (Fig. 4).

Using three-component accelerometric DMG data, the characteristics of the wavefield are analyzed in time–frequency, both for the amplitude spectra using Stockwell *et al.* (1996) decomposition (called *S*-transform [ST]; Fig. 4a,b,f,g) and for the polarization attribute spectra (Fig. 4c–e,h–j) based on Pinnegar (2006). The model assumes that the ground motion at a specific time and frequency can be considered as an elliptical motion confined in a plane. The polarization attributes used in this study to characterize the elliptical motion are the ellipticity and the orientation of the polarization plane.

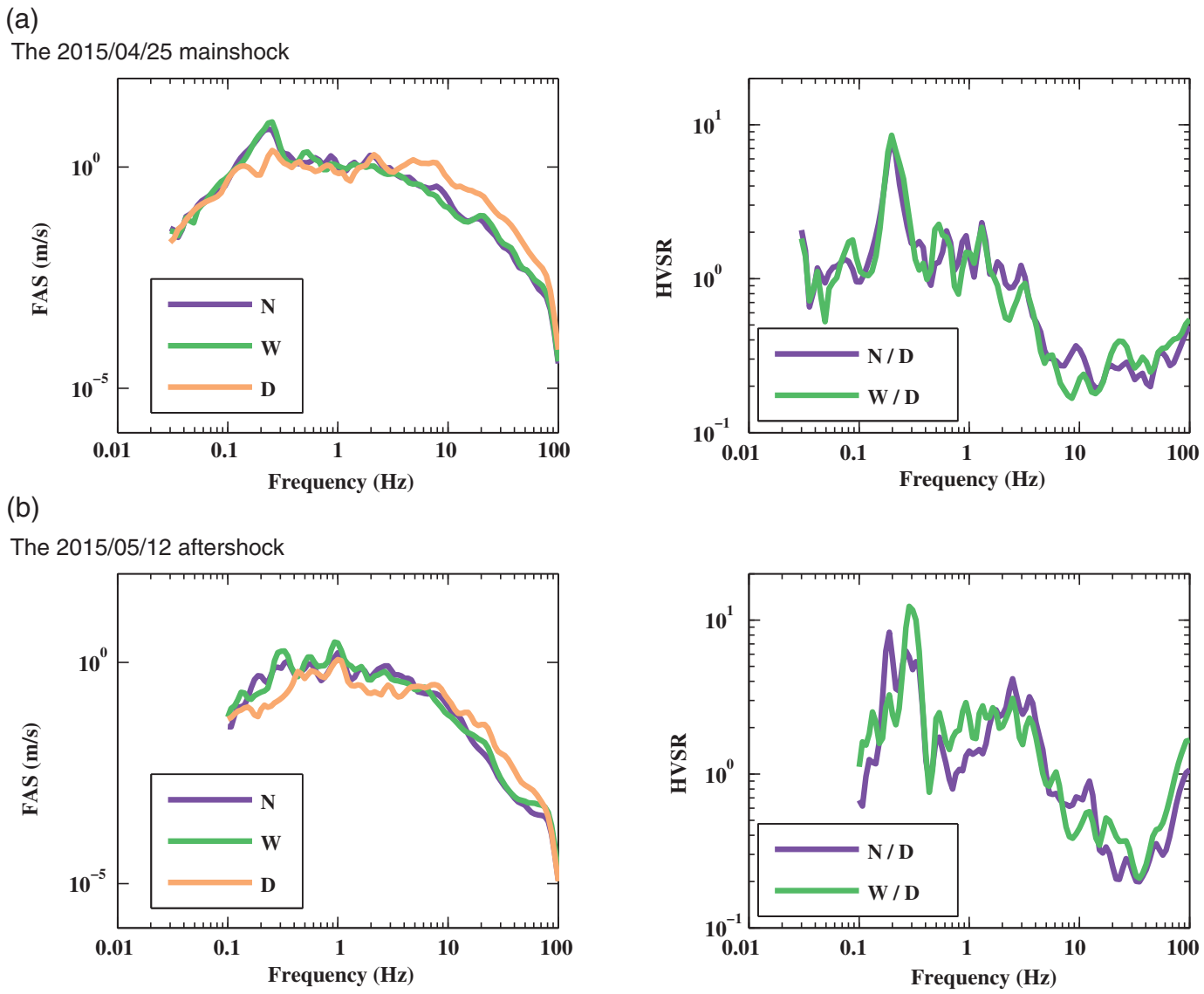

▲ **Figure 3.** (left) Fourier acceleration spectra (FAS) and (right) horizontal-to-vertical spectral ratios (HVSRs) for the two main events. FAS are smoothed according to the Konno and Ohmachi (1998) smoothing with $b = 30$. FAS and HVSRs are represented on the frequency band for which the signal is larger than the noise.

The ellipticity is defined as the ratio between the semi-minor axis and the semi-major axis of the main ellipse motion. The ellipticity values range from 0 to 1, with 0 corresponding to pure linear motion and 1 to pure circular motion (Fig. 4c–h). The azimuth and the dip describe the orientation of the polarization plane. The azimuth (Fig. 4d–i) represents the orientation from the north, and the dip (Fig. 4e–j) is the angle from the horizontal plane (0° corresponds to a horizontal plane and 90° to a vertical plane). Opacity is used to highlight significant amplitudes.

Considering the mainshock (Fig. 4a–e), two separate frequency behaviors are observable: below and above 1 Hz. The low-frequency part (below 1 Hz) on the horizontal components of the ST is dominated by a peak of amplitude around 0.25 Hz (Fig. 4a). This peak is less energetic on the vertical component (Fig. 4b). Around this frequency of 0.25 Hz, the ellipticity is close to 1 from 12 to 40 s (Fig. 4c), meaning that the particle motion is almost circular. After 40 s, the ellipticity becomes close to 0, corresponding to a linear particle motion.

At high frequencies (above 1 Hz), the amplitude is mainly concentrated on the vertical component (Fig. 4b). The waves are all close to linearly polarized motion (ellipticity around 0). It is difficult to determine the actual nature of the wavefield (body or surface waves) without velocity information. Three large, high-frequency energetic arrivals appear around 2 Hz at 26, 32, and 44 s (Fig. 4c–e). The two first arrivals at 26 and 32 s are confined in nearly vertical polarization planes with an azimuth of 40° from north. The polarization of the last arrival at

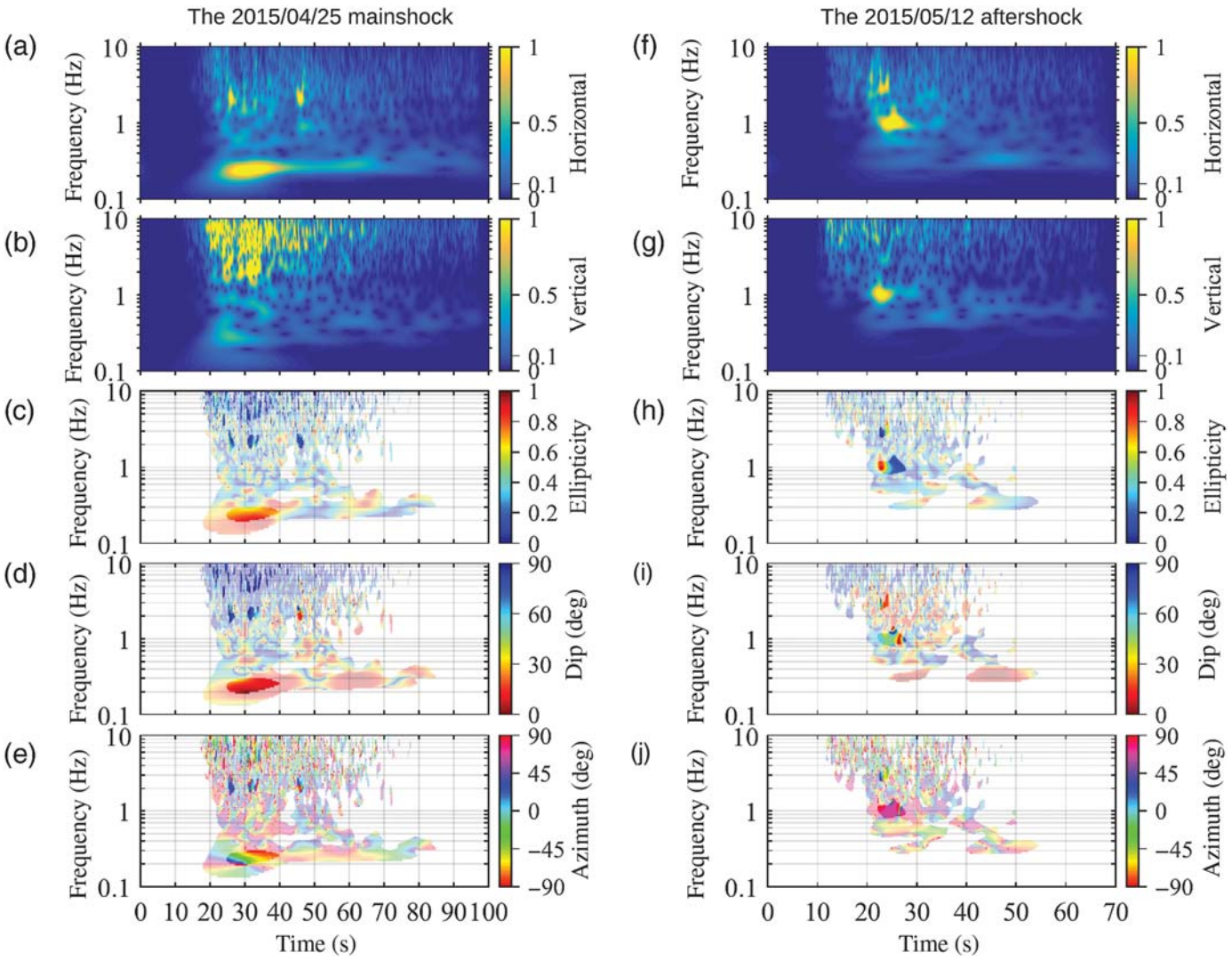

▲ **Figure 4.** Analysis of the mainshock event (on the left) and the aftershock (on the right). (a) and (f) Amplitude of the *S*-Transform (ST) of the horizontal components normalized by the maximum of the total amplitude, defined as $\mathrm{ST}_{\max} = \max_{t,f}[\frac{1}{3}\sqrt{\mathrm{ST}_N(t,f)^2 + \mathrm{ST}_W(t,f)^2 + \mathrm{ST}_D(t,f)^2}]$; (b) and (g) amplitude of the ST of the vertical component normalized by $\mathrm{ST}_{\max}$ (note that the amplitude values above 1 may be clipped by the color scale in some places, leading to some yellow patches); (c) and (h) ellipticity attribute; (d) and (i) dip attribute; (e) and (j) azimuth attribute. In plots (c–e) and (h–j), opacity has been used to highlight the values at which the total amplitude is larger than an arbitrary threshold, lighter colors are for values between 0.1 and 0.5, and brighter colors are for values above 0.5.

44 s is nearly horizontal. This last energetic arrival at 44 s on the horizontal component corresponds to the pulse observed only on the north component of the acceleration-time history (Fig. 2).

The rupture surface of the aftershock was located at a larger distance from Kathmandu than the rupture surface of the mainshock, therefore *P*- and *S*-wave arrivals become distinguishable from each other. The *P* waves, arriving around 10 s, are mainly represented on the vertical component and are dominated by high frequency between 2 and 10 Hz (Fig. 4f,g). The *S* waves arrive around 20 s and have a broader frequency content from 0.25 to 10 Hz. The time–frequency representations are dominated by two peaks of energy, both around 22 s at 1 and 3 Hz (Fig. 4h–j). The peak of energy at 3 Hz is concentrated on the horizontal component, whereas the peak at 1 Hz is polarized with a dip of 45° and with an azimuth of 60°. This peak at 1 Hz is noticeable on the three components and is not observable on the mainshock, meaning that it is probably due to a source effect.

We obtain similar time–frequency results for NQ.KATNP (see Ⓔ Fig. S3), providing a confirmation of the fidelity of both recordings.

Preliminary Discussion about Site Effects

Previously, the work of Paudyal *et al.* (2012) discussed site effects in the Kathmandu basin. Unfortunately, the signal

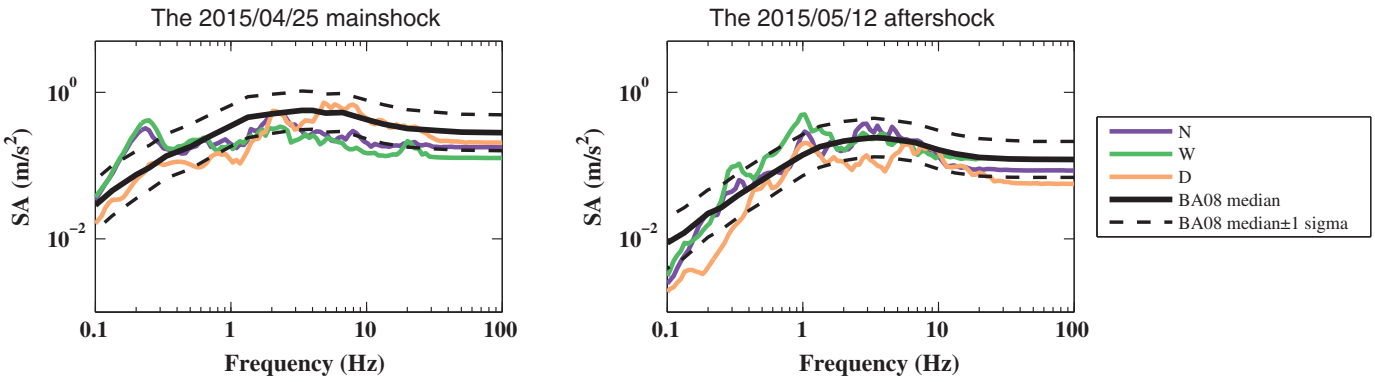

▲ **Figure 5.** Response spectral accelerations with a damping of 5% in meters/square second of the 25 April M_w 7.8 mainshock and of the 12 May M_w 7.3 aftershock, compared with the ground-motion prediction equations of Boore and Atkinson (2008; referred to as BA08). The following input parameters are used: (left) for the mainshock, $M_w = 7.8$, $R_{JB} = 15$ km, $V_{S30} = 250$ m/s, and RS = 1; and (right) for the aftershock, $M_w = 7.3$, $R_{JB} = 65$ km, $V_{S30} = 250$ m/s, and RS = 1, in which RS refers to thrust/reverse fault type.

processing choices did not allow investigation of signals below 0.5 Hz. In this study, the analysis reveals a large, low-frequency amplification: that is, a clear peak at 0.2 Hz for the mainshock and a slightly more diffuse frequency amplification between 0.2 and 0.3 Hz for the aftershock. The observed predominant frequencies are consistent both with the site response estimates of Galetzka *et al.* (2015) and Dixit *et al.* (2015) and with the dominant frequency observed for NQ.KATNP (Ⓔ Figs. S2 and S3).

The differences of predominant frequency between the mainshock and the aftershock could be explained by geometric effects (e.g., Kawase, 1996). Indeed, the Kathmandu basin has a complex geometric shape (Sakai, 2001). These two events have two different azimuths; and, for the aftershock, HVSRs display differences between the two horizontal components. In addition, the second pulse, observed mainly on the north component for the two events and at the two stations (DMG and NQ.KATNP), could be diffracted waves.

Otherwise, the observed differences in terms of frequency could indicate some potential nonlinear site effects, as suggested by Dixit *et al.* (2015) and as has been inferred for other large earthquakes (e.g., Chin and Aki, 1991; Field *et al.*, 1997; Bonilla *et al.*, 2011). Nonlinear site effects are characterized by a decrease in frequency of the predominant peak with the PGA (Beresnev and Wen, 1996).

A more advanced study is required to fully understand the nature of site effects. It seems necessary to process a larger number of events with different characteristics in terms of magnitude, distance, PGA, and azimuth to detect any potential basin edge effects and/or nonlinear effects.

RESPONSE SPECTRA AND COMPARSION WITH PREDICTION

The reference papers for the seismic-hazard assessment in Nepal are National Society for Earthquake Technology (2001) and JICA (2002). A recent global probabilistic seismic-hazard analysis study of Chaulagain *et al.* (2015) predicts, with 10% probability of exceedance in 50 years for the Kathmandu metropolitan city, a PGA around 0.3*g* and a maximum response spectrum of 0.65*g* around 0.2 s.

The acceleration response spectra with a damping of 5% are computed and compared with the prediction from the empirical model of Boore and Atkinson (2008) (Fig. 5). The Boore and Atkinson (2008) ground-motion prediction equation (GMPE) is developed from the Next Generation Attenuation database, composed of worldwide data from active crustal regions. This model has the advantage of well representing the physics of the phenomenon (e.g., nonlinearity with the magnitude, nonlinearity of the geometric attenuation, and nonlinearity of the site) with only few input parameters (M_w, R_{JB}, V_{S30}, and the style of faulting). The Joyner–Boore distance (R_{JB}) parameter, defined as the shortest distance from a site to the surface projection of the rupture surface, must be estimated. A distance of 15 km is used for the mainshock (following the Galetzka *et al.*, [2015] rupture model) and a distance of 65 km is used for the aftershock (following the rupture model of CEA, 2015).

A GMPE obtained from different types of sites represents an average spectral acceleration for a given V_{S30}. The comparison of a GMPE with a real response spectrum highlights the characteristics of a specific site. The two horizontal observed response spectra are generally in good agreement with the prediction within ±1 sigma (Fig. 5). For the mainshock, the observed PGA (0.15*g*) occurs in the lowest part of the predicted distribution, that is, lower than the predicted median (0.27*g*). Thus, this comparison indicates that mainshock was only moderate for the magnitude and distance. However, the response spectra from DMG reveal some amplification peaks with amplitudes larger than the Boore and Atkinson (2008) GMPE. For example, the response spectrum of the mainshock shows a huge amplification at 0.25 Hz.

CONCLUSION

This article presents a preliminary analysis of the acceleration-time histories of the 25 April M_w 7.8 earthquake and its main aftershock of the 12 May M_w 7.3. These time histories are recorded at the station DMG located in Kathmandu under the responsibility of NSC. The comparison with Boore and Atkinson (2008) GMPE indicates that the Gorkha earthquake was only moderate for the magnitude and distance.

The Kathmandu basin is composed of soft sediments with a thickness of about 500 m at the DMG accelerometric station. The rheological contrast between sediments and the bedrock has contributed to amplify the low-frequency ground motions coming from the rupture of the mainshock. During the mainshock, most of the buildings in Kathmandu did not suffer from the low-frequency ground motions because the buildings are not high enough to be affected.

Our time history analysis reveals a particular frequency content with high amplification of the horizontal components around 0.25 Hz for the mainshock and around 0.3 Hz for the aftershock. For the mainshock, the maximum corresponds to circular waves in a horizontal plane. Unfortunately, the comparison with previous site-effect studies is limited because past studies did not consider data below 0.5 Hz. To better understand the frequency content associated with these two events, a more detailed site response analysis would be required.

ACKNOWLEDGMENTS

The authors are most grateful to Sarbajit Prasad Mahato, Director General of the Department of Mines and Geology (DMG) and Soma Nath Sapkota, head of the Geosciences Division, as well as to all the staff of the National Seismological Center of Nepal (NSC) and Département Analyse, Surveillance, Environnement (DASE) who have contributed to this project. Eric Sauvage is particularly thanked for his assistance, as is Sudhir Rajaure for his exchanges at the beginning of the project. Specific thanks to L. Bollinger for discussion about this article. We are grateful to S. Gaffet at Laboratoire Souterrain à Bas Bruit (LSBB), France, for helpful discussion and support on the polarization method. We are also grateful to Susan Hough and an anonymous reviewer for their comments that helped to improve this article.

REFERENCES

Ader, T., J.-P. Avouac, J. Liu-Zeng, H. Lyon-Caen, L. Bollinger, J. Galetzka, J. Genrich, M. Thomas, K. Chanard, S. N. Sapkota, *et al.* (2012). Convergence rate across the Nepal Himalaya and interseismic coupling on the Main Himalaya thrust: Implications for seismic hazard, *J. Geophys. Res.* **117,** no. B04403, doi: 10.1029/2011JB009071.

Adhikari, L. B., U. Gautam, B. P. Koirala, M. Bhattarai, T. Kandel, R. M. Gupta, C. Timsina, N. Maharajan, K. Maharajan, T. Dahal, *et al.* (2015). The aftershock sequence of the April 25 2015 Gorkha-Nepal earthquake, *Geophys. J. Int.* (submitted).

Arias, A. (1970). A measure of earthquake intensity, in *Seismic Design for Nuclear Power Plants*, MIT Press, Cambridge, Massachusetts, 438–483.

Avouac, J.-P., L. Meng, S. Wei, T. Wang, and J.-P. Ampuero (2015). Lower edge of locked Main Himalayan Thrust unzipped by the 2015 Gorkha earthquake, *Nature Geosci.*, **8,** doi: 10.1038/ngeo2518.

Beresnev, I. A., and K. L. Wen (1996). Nonlinear site response—A reality? *Bull. Seismol. Soc. Am.* **86,** 1964–1978.

Bettinelli, P., J.-P. Avouac, M. Flouzat, F. Jouanne, L. Bollinger, P. Willis, and G. R. Chitrakar (2006). Plate motion of India and interseismic strain in the Nepal Himalaya from GPS and DORIS measurements, *J. Geodes.* **80,** 567–589.

Bhattarai, M., U. Gautam, R. Pandey, L. Bollinger, B. Hernandez, and V. Boutin (2011). Capturing first records at the NSC accelerometric network, Nepal, *J. Nepal Geol. Soc.* **43,** 15–22.

Bommer, J., P. Stafford, and J. Alarcón (2009). Empirical equations for the prediction of the significant, bracketed, and uniform duration of earthquake ground motion, *Bull. Seismol. Soc. Am.* **99,** no. 6, 3217–3233, doi: 10.1785/0120080298.

Bonilla, L. F., K. Tsuda, N. Pulido, J. Régnier, and A. Laurendeau (2011). Nonlinear site response evidence of K-NET and KiK-net records from the 2011 Off the Pacific Coast of Tohoku earthquake, *Earth Planets Space* **63,** 785–789.

Boore, D., and G. Atkinson (2008). Ground-motion prediction equations for the average horizontal component of PGA, PGV, and 5%-damped PSA at spectral periods between 0.01 s and 10.0 s, *Earthq. Spectra* **24,** no. 1, 99–138, doi: 10.1193/1.2830434.

Brune, J. (1970). Tectonic stress and the spectra of seismic shear waves from earthquakes, *J. Geophys. Res.* **75,** no. 26, 4997–5009.

Brune, J. (1971). Correction (to Brune, 1970), *J. Geophys. Res.* **76,** 5002.

Chaulagain, H., H. Rodrigues, V. Silva, E. Spacone, and H. Varum (2015). Seismic risk assessment and hazard mapping in Nepal, *Nat. Hazards* **78,** 583–602.

Chin, B. H., and K. Aki (1991). Simultaneous determination of source, path and recording site-effects on strong ground motion during the Loma Prieta earthquake—A preliminary result on pervasive nonlinear site effect, *Bull. Seismol. Soc. Am.* **81,** 1859–1884.

Commissariat à l'énergie atomique et aux énergies alternatives (CEA), *Nepal Earthquakes of 25 April and 12 May 2015*, http://www-dase.cea.fr/actu/dossiers_scientifiques/2015-05-12/index_en.html (last accessed September 2015).

Dixit, A. M., A. Ringler, D. Sumy, E. Cochran, S. E. Hough, S. S. Martin, S. Gibbons, J. Luetgert, J. Galetzka, S. N. Shrestha, *et al.* (2015). Strong-motion observations of the M 7.8 Gorkha, Nepal, earthquake sequence and development of the N-SHAKE strong-motion network, *Seismol. Res. Lett.* **86,** no. 6, doi: 10.1785/0220150146.

Field, E. H., P. A. Johnson, I. A. Beresnev, and Y. Zeng (1997). Nonlinear ground-motion amplification by sediments during the 1994 Northridge earthquake, *Nature* **390,** no. 6660, 599–602.

Galetzka, J., D. Melgar, J. F. Genrich, J. Geng, S. Owen, E. O. Lindsey, X. Xu, Y. Bock, J.-P. Avouac, L. B. Adhikari, *et al.* (2015). Slip pulse and resonance of Kathmandu basin during the 2015 Gorkha earthquake, Nepal, *Science* **349,** no. 6252, 1091–1095.

Goda, K, T. Kiyota, R. Pokhrel, G. Chiaro, T. Katagiri, K. Sharma, and S. Wilkinson (2015). The 2015 Gorkha Nepal earthquake: Insights from earthquake damage survey, *Front. Built Environ.* **1,** 8, doi: 10.3389/fbuil.2015.00008.

Government of Nepal (2015). *Nepal Disaster Risk Reduction Portal*, http://drrportal.gov.np/ (last accessed June 2015).

Husid, R. (1969). Analisis de terremotos: Analisis general, *Revista del IDIEM* **8,** no. 1, 21–42 (in Spanish).

Japan International Cooperation Agency (2002). *The Study on Earthquake Disaster Mitigation in the Kathmandu Valley Kingdom of Nepal*, Japan International Cooperation Agency (JICA) and Ministry of Home Affairs His Majesty's Government of Nepal, Vols. I–III, Nippon Koei Co., Ltd., Oyo Corporation.

Jouanne, F., J. L. Mugnier, J. F. Gamond, P. L. Fort, M. R. Pandey, L. Bollinger, M. Flouzat, and J. P. Avouac (2004). Current shortening across the Himalayas of Nepal, *Geophys. J. Int.* **157,** 1–14.

Kawase, H. (1996). The cause of the damage belt in Kobe: "The basin-edge effect," constructive interference of the direct S-wave with the basin-induced diffracted/Rayleigh waves, *Seismol. Res. Lett.* **67,** no. 5, 25–34.

Konno, K., and T. Ohmachi (1998). Ground-motion characteristics estimated from spectral ratio between horizontal and vertical components of microtremor, *Bull. Seismol. Soc. Am.* **88,** no. 1, 228–241.

Lavé, J., and J.-P. Avouac (2000). Active folding of fluvial terraces across the Siwaliks Hills, Himalayas of central Nepal, *J. Geophys. Res.* **105,** 5735–5770.

Lermo, J, and F. J. Chavez-Garcia (1993). Site effect evaluation using spectral ratios with only one station, *Bull. Seismol. Soc. Am.* **83,** no. 5, 1574–1594.

Martin, S. S., S. E. Hough, R. Bilham, and C. Hung (2015). Ground motions from the 2015 M_w 7.8 Gorkha, Nepal, earthquake, constrained by a detailed assessment of macroseismic data, *Seismol. Res. Lett.* **86,** no. 6, doi: 10.1785/0220150138.

Nakamura, Y. (1989). A method for dynamic characteristics estimation of subsurface using microtremor on the ground surface, *Q. Rep. Railway Tech. Res. Inst.* **30,** 25–33.

National Society for Earthquake Technology (2001). The Kathmandu Valley Earthquake risk management action plan, a product of the Kathmandu Valley Earthquake Risk Management Project, http://www.nset.org.np/nset2012/images/publicationfile/20111220133210.pdf (last accessed September 2015).

Paudyal, Y. R., N. P. Bhandary, and R. Yatabe (2012). Seismic microzonation of densely populated area of Kathmandu Valley of Nepal using microtremor observations, *J. Earthq. Eng.* **16,** no. 8, 1208–1229.

Pinnegar, C. R. (2006). Polarization analysis and polarization filtering of the three-component signals with the time-frequency *S* transform, *Geophys. J. Int.* **165,** 596–606

Sakai, H. (2001). Stratigraphic division and sedimentary facies of the Kathmandu basin sediments, *J. Nepal Geol. Soc.* **25,** 19–32.

Stockwell, R. G., L. Mansinha, and R. P. Lowe (1996). Localization of the complex spectrum: The S-transform, *IEEE Trans. Signal Process.* **44,** no. 4, 998–1001.

United States Geological Survey (USGS), http://earthquake.usgs.gov/earthquakes/eventpage/us20002926#general_summary (last accessed June 2015).

Wald, D. J., and T. I. Allen (2007). Topographic slope as a proxy for seismic site conditions and amplification, *Bull. Seismol. Soc. Am.* **97,** no. 5, 1379–1395.

M. Bhattarai
L. B. Adhikari
U. P. Gautam
National Seismological Centre
Department of Mines and Geology
Lainchaur
Kathmandu, Nepal
mukunda.research@gmail.com

A. Laurendeau
***C. Labonne*[1]**
***R. Hoste-Colomer*[2]**
O. Sèbe
B. Hernandez
Commissariat Energie Atomique
Direction des Applications Militaires (DAM)
Direction Ile de France (DIF)
F-91297 Arpajon, France

[1] Also at Université Nice Sophia Antipolis, National Centre for Scientific Research (CNRS) L'Institut de recherche pour le développement (IRD), Geoazur UMR 7329, Observatoire de la Côte d'Azur, Valbonne, France.
[2] Also at Laboratoire de Géologie, Ecole Normale Supérieure, CNRS, 24 rue Lhomond, 75004 Paris, France.